

# 3 EXPERIMENTAL

## 3.1 PULSE GENERATION

In our experiments we use ultrashort laser pulses of  $<150$  fs in the visible region (400-800 nm) and in the mid-infrared region between 3 and 7  $\mu\text{m}$  (1500-3000  $\text{cm}^{-1}$ ). To create these pulses we use a series of non-linear techniques to convert light from a commercial Ti:sapphire regenerative amplifier system (Quantronix Titan) into the desired wavelengths. The amplifier itself is seeded by an oscillator (Spectra Physics Tsunami) that delivers 800 nm pulses with FWHM  $\sim 17$  nm at a repetition rate of 80 MHz. These seed pulses are stretched using a set of gratings and amplified at a 1 kHz rate in Ti:sapphire crystals that are pumped with the output from an intra-cavity doubled, Nd:YLF laser system (Quantronix Falcon). The amplification consists of a regenerative amplification cavity that is controlled with a Pockels cell. This amplification is followed by a multi-pass amplification stage with a second pumped Ti:sapphire crystal. The final result after compression are  $\sim 100$  fs 800 nm pulses with pulse energies of 3 mJ at a 1 kHz repetition rate.

To create 400 nm pump pulses, we use second-harmonic generation of part of the 800 nm light in a  $\beta$  barium borate (BBO) crystal. To create visible probe light, we broaden the spectrum of 800 nm pulses with self-phase modulation by focussing them into a sapphire crystal. The infrared pump and probe pulses are created according to the schematic shown in Fig. 3.1. We use parts of the 800 nm light to pump two separate BBO based Optical Parametric Amplifiers (OPA). The OPAs split the 800 nm pulses into lower frequency signal and idler pulses through a series of white light or super-fluorescence seeded parametric amplification stages. We create pump pulses in the frequency regions around 3 and 4  $\mu\text{m}$  by frequency doubling the idler pulses in a BBO crystal and parametrically amplifying these doubled idler pulses with 800 nm pump pulses in either Potassium Titanyl Phosphate (KTP) or Potassium Niobate crystals (KN). Infrared probe pulses in the frequency regions between 3 and 7  $\mu\text{m}$  are created using difference frequency generation between signal and idler pulses in a silver gallium disulfide (AGS) crystal. The pump and probe pulses had typical pulse energies of 5  $\mu\text{J}$  and 20 nJ, respectively.

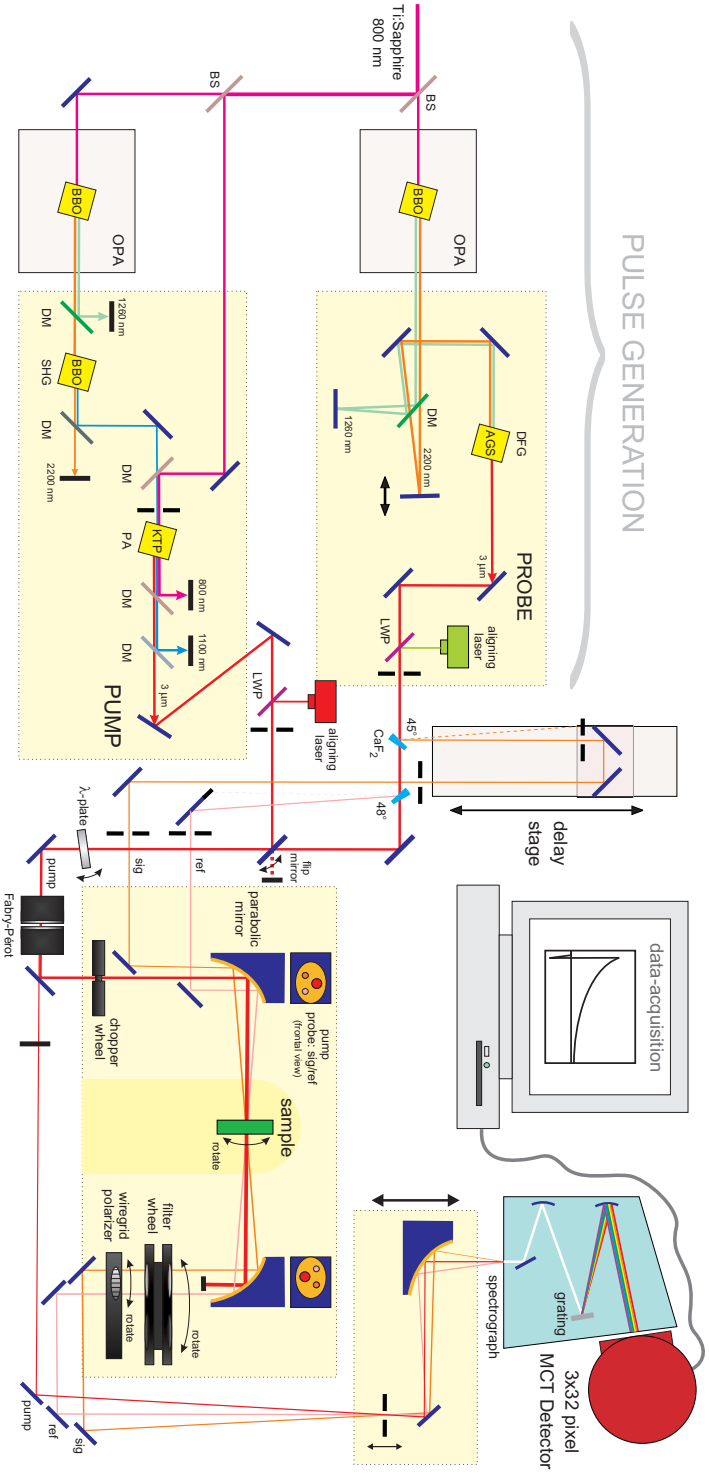


FIGURE 3.1. Infrared two-color pump-probe setup. 800 nm light from a Ti:Sapphire laser system is split in three parts using Beam Splitters (BS). Two parts are used to pump two separate Optical Parametric Amplifiers (OPA). These split the 800 nm light in signal and idler pulses using Parametric Amplification (PA) of either white-light or a super-fluorescence seed. Pump light is generated by Second Harmonic Generation of the idler followed by Parametric Amplification with 800 nm. Probe light is generated by Difference Frequency Generation (DFG) of signal and idler. Dichroic Mirrors (DM) and Long Wave Pass (LWP) filter out unwanted frequencies. The probe light is split into a probe and a reference beam using  $\text{CaF}_2$  wedged windows. The probe beam is time-delayed with respect to the pump; the reference always precedes the pump. Half of the pump pulses are blocked by a Fabry-Pérot chopper wheel. The pump polarization is rotated with a  $\lambda/2$ -plate. The pump frequency can be tuned by a Fabry-Pérot interferometer. The pump, probe, and reference are spatially overlapped and focussed by a parabolic mirror in the sample cell. The intensity of the probe and the reference are tuned with a filter wheel, and different polarization components are selected with a rotating polarizer. Probe, reference, and optionally pump are dispersed by a spectrograph and measured with a  $3 \times 32$  pixel Mercury Cadmium Telluride (MCT) detector by data acquisition software. The data acquisition controls the delay-stage, Fabry-Pérot, spectrograph, and rotating polarizer.

## 3.2 PUMP-PROBE SETUP

The infrared two-color pump-probe setup that was used in most of the experiments is shown in Fig. 3.1 including pulse generation, pump-probe overlap and signal detection. The pulse generation part of the setup was varied slightly depending on the frequencies needed for the experiments. The basic pump-probe scheme involves the spatial overlap of two beams, pump and probe, inside the sample under study. The beams are focussed inside the sample to maximize the pump-probe signal. The relative polarization between pump and probe is either at magic angle ( $54.7^\circ$ ), for rotation-free measurements, or  $45^\circ$ , for polarization-resolved measurements. In the latter case a rotating polarizer selects parallel and perpendicular components of the probe after the sample. We split part of the probe before the sample which acts as a reference beam to correct for pulse-to-pulse fluctuations as explained in Section 4.1. The temporal overlap of pump and probe pulses is controlled with a delay stage.

## 3.3 SAMPLE CELL

The basic sample cell consists of a static construction which holds two calcium-fluoride windows together, separated by a teflon spacer to provide an optical path length between 10–500  $\mu\text{m}$ . The sample cell holder and one of the windows provides a pair of small openings to allow for the easy exchange of different liquid samples. The standard procedure for sample replacement consists of an extensive flush by the sample solvent, followed by a flush with the new sample. This method is preferred when performing a comparative series of measurements where a particular aspect of the sample, such as the concentration, is varied. It ensures that the measured samples have the same optical path length.

For experiments that are influenced by steady state heating of the sample we use a rotating sample-cell. The main disadvantage of a rotating sample cell is the introduction of noise through either the scattering off the windows or the wobbling around the pump-probe focus overlap. Also, great care has to be taken that the thickness of the sample cell is uniform along the rotation path. This and the slightly more cumbersome procedure needed to replace samples, is why the static cell is usually preferred.

Temperature-dependence measurements in the region  $\sim 5\text{--}70^\circ\text{C}$  are performed using a sample cell with a (thermoelectric) Peltier element. The more advanced version of this cell also allows for circular rotation. For cryogenic experiments we use a closed-cycle liquid-helium cooled cryostat. The cryostat weighs about 25 kg and is connected to a liquid helium reservoir and a vacuum pump system. The vacuum jacket of the cryostat is equipped with two calcium fluoride windows which allows optical access to the sample. For experiments that require rotation of the cryogenic sample we designed a 'cryostat rotator' as shown in Fig. 3.2.

This cryostat-rotator is mounted on a frame independent of the laser table to prevent it from influencing the vibration sensitive laser setup. This suspended

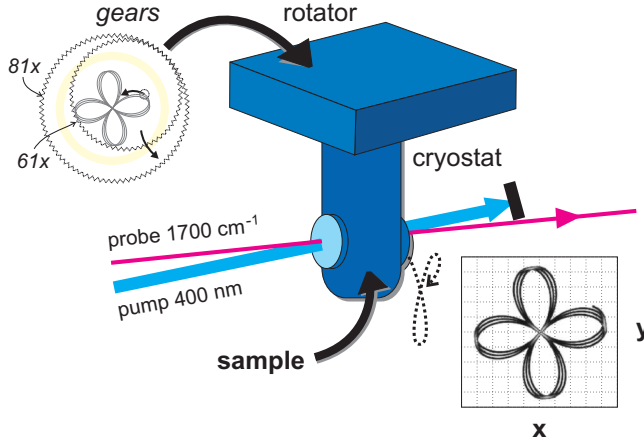


FIGURE 3.2. The middle part shows a schematic depiction of the cryostat rotator hanging in the pump-probe setup. The top left shows the outer and inner gears that together create the hypotrochoid trajectory, resulting in a period of almost five thousand rotations. The bottom right picture shows a simulation of the pump intensity distribution across the sample after a few rotations.

device is capable of moving around the entire cryostat including the attached hoses while keeping the sample within the focal length of the probe ( $\sim 1$  mm). To achieve maximum spread of the pump beam across the sample and minimize photo-damage we use a pair of inner and outer gears and rotated the sample along a hypotrochoid trajectory. The  $x$  and  $y$  positions of this trajectory at time  $t$  at an angular speed  $\omega$  can be described by the following set of parametric equations:

$$x(t) = (R - r) \cos(\omega t) + \delta \cos\left(-\frac{R - r}{r} \omega t\right), \quad (3.1)$$

$$y(t) = (R - r) \sin(\omega t) + \delta \sin\left(-\frac{R - r}{r} \omega t\right). \quad (3.2)$$

Here  $R$  and  $r$  are the radii of the outer and inner gears, respectively, and  $\delta$  is the offset from the center of the inner wheel to which the rotating cryostat is attached. The number of teeth on the two gears were chosen to be relative prime (61 and 81) in order to achieve the maximum possible period before the trajectory turns back on itself, i. e. after  $61 \times 81 = 4941$  rotations. Part of the trajectory is shown in Fig. 3.2. This device provides us the necessary time of sometimes up to six hours per measurement to achieve satisfactory signal to noise ratios for experiments on ice.

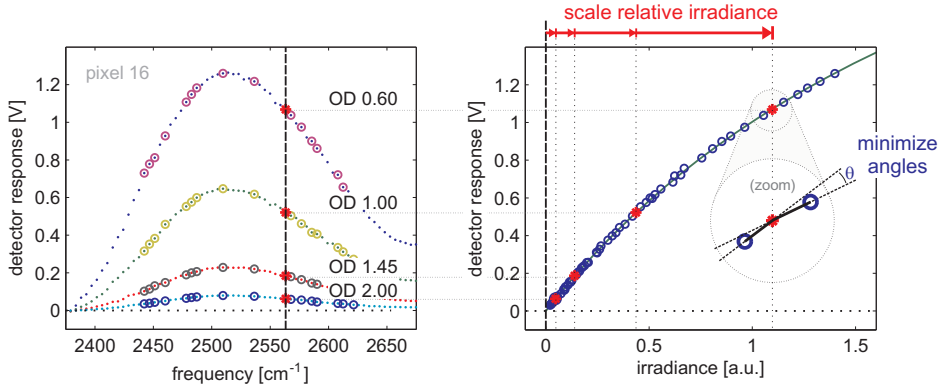


FIGURE 3.3. Detector response and calibration curves for a single pixel. Left: The detector voltages measured for different frequencies of the probe pulse and for different optical density filters. Right: Voltage response as a function of pulse intensity and the fitted calibration curve. Zoom inset shows angles between subsequent line pieces that are minimized by scaling the relative irradiances.

### 3.4 DETECTOR

The Mercury Cadmium Telluride (MCT) infrared pixel-detector, amplification, and data-processing result in a frequency-resolved voltage measurements that should reflect the intensity of the probe pulses through the sample. Ideally this voltage  $V$  linearly depends on the incident pulse energy  $I$ , however this was not found to be the case. First of all, we correct for zero-point drift of the detector voltages by periodic dark voltage measurements with a closed detector shutter. Because the pump-probe signal is always a relative intensity ( $T/T_0$ ), the linear sensitivity of the detector has no influence on it. However, a non-linearity of the detector response causes noticeable deviations, e.g. when there is a large variation in intensities over the probe spectrum.

To correct for this non-linearity we need to find a calibration function  $I(V)$  that returns the intensity of the incident laser pulse for a measured detector voltage  $V$  (see Fig. 3.3). In principle, this function can be retrieved by shining a selection of known intensities onto the detector and measuring the resulting voltages. In practice, this would be cumbersome as each point on the curve  $V_i(I_i)$  needs to be measured separately, e.g. by using a discrete set of filters with known relative optical densities. Instead we proceed as follows.

Infrared probe light with the desired frequency-dependent intensity spectrum  $I(\nu)^a$  is generated and coupled into the spectrograph. The spectrum should contain intensities that result in the desired range of voltages for which the detector needs to be calibrated. By rotating the spectrograph grating we scan the probe spectrum and record the frequency dependent resulting voltages

<sup>a</sup>in the remainder of this thesis we express the frequency in [ $\text{cm}^{-1}$ ] with the symbol  $\nu = \omega/200\pi c$

$V(\nu)$  separately for all pixels of the detector. This spectrograph scan is repeated for  $d$  different relative intensities by changing the optical density (OD) of filters placed in the probe path (filter wheel Fig. 3.1). We thus record for each pixel a set of voltage spectra  $V_d(\nu)$  whose intensities scale as

$$I(V_d(\nu)) = I_0(\nu) \times 10^{-OD_d}, \quad (3.3)$$

At this point we do not know the values of  $I_0(\nu)$ , only the resulting spectra  $V_d(\nu)$  for different filters  $d$ . Because we are only interested in relative values of  $I_0$  we start by setting  $I_0(\nu_i) = 1$  for any particular frequency  $\nu_i$ . We thus find as the starting points for the calibration curve  $V = V_d(\nu_i)$  as a function of  $I = 10^{-OD_d}$ . The algorithm proceeds by choosing a different frequency  $\nu_j$  with different voltages  $V_d(\nu_j)$  and scales  $I_0(\nu_j)$  such that the resulting values of  $V_d(\nu_j)$  together with the previously obtained values  $V_d(\nu_i)$  form a bijective function of  $I$ , i. e. the calibration curve is a one-to-one correspondence between  $I$  and  $V$ . This scaling involves a chi-squared minimization of the angles between subsequent lines pieces as shown in Fig. 3.3. Additional frequencies are chosen and the procedure is iterated until a satisfactory range of voltages is covered. The advantage of this method is, that no assumptions have thus far been made about the functional form of the calibration curve. After the calibration was complete we found that its form was well described with the function

$$I = \frac{p V}{1 - V/V_{\max}}, \quad (3.4)$$

where  $p$  is an arbitrary scaling constant that reflects the absolute sensitivity of the detector pixels and  $V_{\max}$  is the saturation voltage of the pixel. The procedure is repeated for all pixels of the detector and the scaling constants  $p$  are chosen such that differences in pixel-to-pixel sensitivity are compensated and their average value  $\sum_{n=1}^N p_n/N = 1$ . In the case of small transmission changes, these pixel-to-pixel sensitivities  $p$  have no influence on the dynamics of pump-probe measurements but are useful e. g. for the determination of spectral shapes.